# Multidimensional thermal analysis of an ultrawide bandgap AlGaN channel high electron mobility transistor

Cite as: Appl. Phys. Lett. **115**, 153503 (2019); https://doi.org/10.1063/1.5115013 Submitted: 13 June 2019 . Accepted: 22 September 2019 . Published Online: 09 October 2019

James Spencer Lundh (D), Bikramjit Chatterjee (D), Yiwen Song, Albert G. Baca (D), Robert J. Kaplar (D), Thomas E. Beechem, Andrew A. Allerman, Andrew M. Armstrong (D), Brianna A. Klein, Anushka Bansal (D), Disha Talreja, Alexej Pogrebnyakov (D), Eric Heller (D), Venkatraman Gopalan, Joan M. Redwing (D), Brian M. Foley, and Sukwon Choi (D)







## ARTICLES YOU MAY BE INTERESTED IN

Intersubband resonant enhancement of second order-nonlinear susceptibility in asymmetric Al<sub>x</sub>Ga<sub>1-x</sub>N/GaN double quantum wells

Journal of Applied Physics 126, 135704 (2019); https://doi.org/10.1063/1.5110176

Study on the charging current of surface traps in AlGaN/GaN high electron mobility transistors with a slot gate structure

Applied Physics Letters 115, 152105 (2019); https://doi.org/10.1063/1.5111494

Characterization of non-linearities through mechanical squeezing in levitated optomechanics Applied Physics Letters 115, 153106 (2019); https://doi.org/10.1063/1.5116121









## Multidimensional thermal analysis of an ultrawide bandgap AlGaN channel high electron mobility transistor

Cite as: Appl. Phys. Lett. **115**, 153503 (2019); doi: 10.1063/1.5115013 Submitted: 13 June 2019 · Accepted: 22 September 2019 · Published Online: 9 October 2019







James Spencer Lundh, 1 Bikramjit Chatterjee, 1 Yiwen Song, 1 Albert G. Baca, 2 Robert J. Kaplar, 2 Thomas E. Beechem, 2 Andrew A. Allerman, 2 Andrew M. Armstrong, 2 Brianna A. Klein, 2 Anushka Bansal, 3 Disha Talreja, 3 Alexej Pogrebnyakov, 3 Eric Heller, 4 Venkatraman Gopalan, 3 Joan M. Redwing, 3 Brian M. Foley, 1 and Sukwon Choil, 2 Eric Heller, 4 Venkatraman Gopalan, 3 Joan M. Redwing, 3 Venkatraman Gopalan, 3 Joan M. Redwing, 5 Venkatraman Gopalan, 5 Joan M. Redwing, 6 Venkatraman Gopalan, 5 Joan M. Redwing, 6 Venkatraman Gopalan, 6 Venkatraman Gopalan, 6 Venkatraman Gopalan, 6 Venkatraman Gopalan, 7 Venkatraman Gopalan, 8 Venkatraman Gopalan, 8 Venkatraman Gopalan, 9 Venkatraman Gopalan, 9

## **AFFILIATIONS**

- $^1$ Department of Mechanical Engineering, The Pennsylvania State University, University Park, Pennsylvania 16802, USA
- <sup>2</sup>Sandia National Laboratories, Albuquerque, New Mexico 87185, USA
- Department of Materials Science and Engineering, The Pennsylvania State University, University Park, Pennsylvania 16802, USA
- <sup>4</sup>Materials and Manufacturing Directorate, Air Force Research Laboratory, Wright-Patterson Air Force Base, Ohio 45433, USA

## **ABSTRACT**

Improvements in radio frequency and power electronics can potentially be realized with ultrawide bandgap materials such as aluminum gallium nitride ( $Al_xGa_{1-x}N$ ). Multidimensional thermal characterization of an  $Al_{0.30}Ga_{0.70}N$  channel high electron mobility transistor (HEMT) was done using Raman spectroscopy and thermoreflectance thermal imaging to experimentally determine the lateral and vertical steady-state operating temperature profiles. An electrothermal model of the  $Al_{0.30}Ga_{0.70}N$  channel HEMT was developed to validate the experimental results and investigate potential device-level thermal management. While the low thermal conductivity of this III-N ternary alloy system results in more device self-heating at room temperature, the temperature insensitive thermal and electrical output characteristics of  $Al_xGa_{1-x}N$  may open the door for extreme temperature applications.

Published under license by AIP Publishing. https://doi.org/10.1063/1.5115013

Wide bandgap (WBG) gallium nitride (GaN) channel high electron mobility transistors (HEMTs) have matured significantly over decades of research, and commercial devices are available from multiple vendors. As such, researchers are investigating pathways for next generation devices through the adoption of ultrawide bandgap (UWBG) materials with bandgaps larger than that of GaN ( $\sim$ 3.4 eV). Al<sub>x</sub>Ga<sub>1-x</sub>N, whose bandgap energy increases with the Al-composition (0 < x < 1), emerges as a natural choice due to the established GaN HEMT technology. Favorable characteristics such as high breakdown field, high saturation velocity, and high temperature operation demonstrate the superior potential of Al<sub>x</sub>Ga<sub>1-x</sub>N for high power switching and radio frequency (RF) applications. <sup>1-3</sup>

For high power switching applications, high breakdown voltages  $(V_B)$  and low specific on-resistances  $(R_{on,sp})$  are required.<sup>4</sup> A lateral figure of merit (LFOM) has been formulated to compare the potential of material systems for power-switching.<sup>3</sup>

$$LFOM = \frac{V_B^2}{R_{on,sp}} = q\mu_{ch}n_sE_c^2,$$

where q is the electronic charge constant,  $\mu_{ch}$  is channel mobility,  $n_s$  is sheet carrier density, and  $E_c$  is the critical electric field. Since the critical electric field scales with the bandgap energy  $(E_c \sim E_g^{\ n},\ 2 < n < 2.5),^5 \ Al_x Ga_{1-x} N$  offers substantial LFOM improvements over GaN at high temperatures. The channel mobility of  $Al_x Ga_{1-x} N$  is relatively low due to disordered alloy scattering, but research to improve  $\mu_{ch}$  of the  $Al_x Ga_{1-x} N$  active layer is ongoing. High specific onresistance is another limitation, but recent studies show promise for improved Ohmic contact technologies, especially at high temperatures. Especially at high temperatures.

For high power RF applications, high breakdown voltages and high cutoff frequencies ( $f_T$ ) are required. <sup>11</sup> The Johnson figure of merit (JFOM) is employed to assess material systems for high frequency operation: <sup>3</sup>

a) Author to whom correspondence should be addressed: sukwon.choi@psu.edu

$$JFOM = V_B f_T = \frac{E_c v_{sat}}{2\pi},$$

where  $v_{sat}$  is the electron saturation velocity. While theoretical studies show slight reductions in  $v_{sat}$  for  $Al_xGa_{1-x}N$  with low/intermediate Al-compositions, the increased critical electric field at higher Al-compositions (allowing shorter channel devices) dominates and improves the JFOM over GaN.<sup>3</sup>

 ${\rm Al_xGa_{1-x}N}$  channel HEMT technology has been advancing over the past few years through continued efforts to improve the electrical performance such as lowering the contact resistance. However, excluding "high temperature testing" involving electrical characterization at elevated base temperatures, <sup>2,12</sup> device-level thermal characterization has been absent. Because  ${\rm Al_xGa_{1-x}N}$  is promising for next generation power and RF electronics, the thermal characteristics and limits of this device technology need exploration.

Similar to GaN HEMTs, device self-heating is expected. Self-heating was studied extensively in GaN HEMTs,  $^{13-16}$  and much research was focused on thermal management.  $^{16-20}$  Likewise, experimental characterization of device self-heating in the  $Al_xGa_{1-x}N$  technology is necessary to lay the groundwork for electrothermal codesign. Unfortunately, the self-heating behavior of  $Al_xGa_{1-x}N$  HEMTs has been unexplored due to challenging experimental limitations. An electrothermal model which reproduces both electrical and thermal device characteristics can be used to design thermal management solutions and test the new device technology for extreme environments. As such, thermal characterization and electrothermal simulation were performed on both  $Al_{0.30}Ga_{0.70}N$  and GaN channel HEMTs for comparison, and thermal management of  $Al_xGa_{1-x}N$  channel HEMTs for high temperature applications is briefly discussed.

The  $Al_{0.30}Ga_{0.70}N$  channel HEMTs<sup>12</sup> (Fig. 1) were grown on 1.3 mm thick sapphire substrates using metal organic chemical vapor deposition (MOCVD). First, a  $1.6\,\mu m$  AlN transition layer was grown followed by a  $3.9\,\mu m$  and  $0.25\,\mu m$  Al $_{0.30}Ga_{0.70}N$  buffer and channel layer, respectively. The structure was capped with a  $50\,n m$  Al $_{0.45}Ga_{0.55}N$  barrier and SiN passivation. The Ohmic contacts were formed using a Ti/Al/Ni/Au (25/100/15/50 nm) metal stack. The gate contact was formed using a Ni/Au Schottky metal stack with  $1\,\mu m$  field plate extensions over the SiN dielectric on the drain and source sides. For some structures, the field plate was slightly misaligned to provide more direct access to the drain side edge of the gate contact

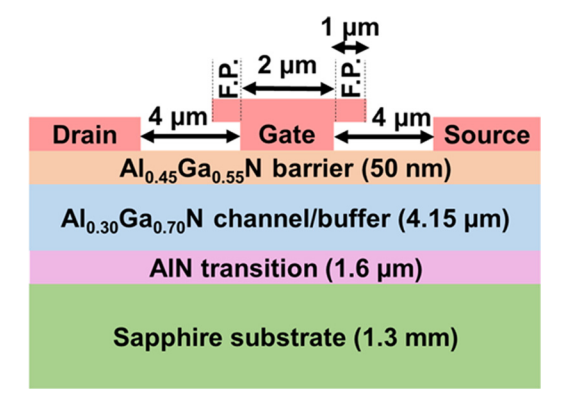


**FIG. 1.** (a) Cross-sectional schematic of the  $Al_{0.30}Ga_{0.70}N$  channel HEMT<sup>12</sup> device structure. Field plate structures are denoted by F.P.

for temperature measurement. This was done because this is the location of peak heat generation due to the localized electric field concentration. The HEMTs have a circular geometry with a gate length of 2  $\mu m$ , gate-drain and gate-source spacings of 4  $\mu m$ , and a gate circumference of 330  $\mu m$ . GaN HEMTs with similar circular device geometries were studied for comparison. The GaN HEMTs were grown on a 650  $\mu m$  thick semi-insulating 6H-SiC substrate with a thin ( $\sim\!50$  nm) AlN transition layer and a 4  $\mu m$  thick GaN buffer. The GaN HEMTs have a gate length of 2  $\mu m$ , a gate-drain spacing of 6  $\mu m$ , a gate-source spacing of 2  $\mu m$ , and a gate circumference of 310  $\mu m$ .

An electrothermal model<sup>23</sup> was developed that couples an electrical model (Synopsys Sentaurus) with a finite element thermal model (COMSOL Multiphysics). Material properties such as bandgap energy, electron mobility, and dielectric constant were adopted from the literature. 1,3 The contact and sheet resistances of the Al<sub>0.30</sub>Ga<sub>0.70</sub>N and GaN channel HEMTs were extracted using transmission line model (TLM) measurements with four-point probing.<sup>24</sup> The temperature dependent thermal conductivity of the Al<sub>0.30</sub>Ga<sub>0.70</sub>N channel/buffer layer was measured using frequency domain thermoreflectance (FDTR),<sup>25</sup> a laser-based optical pump-probe method. The pump laser (405 nm Coherent Obis) is modulated by the lock-in amplifier (Zurich Instruments HF2LI) to produce a square waveform, while the frequency-matched probe laser (532 nm Coherent Obis) is coaxially aligned with the pump to detect the magnitude and phase of the surface temperature relative to the pump laser heating event. By sweeping frequency and measuring the phase difference between the heat flux and the surface temperature, the thermal properties of the Al<sub>0.30</sub>Ga<sub>0.70</sub>N can be determined by fitting the data to a multilayer model. Expected uncertainties in measured values are typically <10%, largely driven by uncertainties in the model input parameters such as heat capacity and layer thickness, as well as error associated with scanto-scan repeatability (laser spot focus and pump/probe beam overlap). The thermal conductivity of the Al<sub>0.30</sub>Ga<sub>0.70</sub>N channel/buffer layer was found to be  $8.5 \pm 0.85 \text{ W/(m*K)}$  at room temperature and with a negligible temperature dependence up to 450 K. To account for potential spatial variations, measurements were made at various locations on the sample.

Thermal characterization was performed using Raman thermometry and thermoreflectance thermal imaging. As demonstrated previously,  $^{26}$  thermoreflectance thermal imaging can acquire 2D thermal maps of device surfaces; it is particularly effective for highly reflective features such as metallization structures and was therefore used to determine the temperatures of the HEMT source, drain, and gate electrodes. Thermoreflectance thermal imaging was performed using a Microsanj NT-210A system with a 3-axis piezocontrolled stage and a  $1626\times1236$  pixel charge coupled device (CCD) camera. A long working distance 50X objective (NA = 0.45) was used, providing a spatial resolution of  $\sim\!0.6~\mu\mathrm{m}$  with 530 nm LED illumination. Using standard calibration procedures,  $^{27}$  point-by-point thermoreflectance coefficient maps of the  $\mathrm{Al}_{0.30}\mathrm{Ga}_{0.70}\mathrm{N}$  HEMT was obtained.

To probe the channel surface temperatures, nanoparticle-assisted Raman thermometry<sup>28</sup> was used. In this technique, the temperature dependence of a particular phonon mode frequency of the deposited nanoparticle is used to determine the device surface temperature since the nanoparticle is assumed to be in thermal equilibrium with the device surface. Since the nanoparticle can expand freely, stress affecting the Raman peak position is assumed to be negligible. From the

authors' previous study, <sup>28</sup> titanium dioxide ( ${\rm TiO_2}$ ) nanoparticles (99.98% purity) were selected due to the good temperature sensitivity of the E<sub>g</sub> phonon frequency and low measurement uncertainty. Nanoparticle-assisted Raman thermometry was performed using a Horiba LabRAM HR Evolution spectrometer with 532 nm excitation. Measurements were performed in a 180° backscattering configuration with a long working distance  $50\times$  objective (NA = 0.45) where the spatial resolution is determined by the size of the submicrometer nanoparticles. To reduce systematic error resulting from sources such as room temperature fluctuations, a reference mercury emission line at  $\sim$ 546 nm was used. The dependence of the  ${\rm TiO_2}$  E<sub>g</sub> frequency on incident laser power was investigated to determine the threshold for laser-induced heating in order to select a suitable laser power ( $\sim$ 1 mW).

To investigate the vertical temperature distribution, confocal Raman thermometry was used. The experimental setup described above offered a spatial resolution of  $\sim 1 \,\mu m$  and a depth of field of  $\sim$ 10  $\mu$ m. For the GaN HEMTs, it was possible to probe the average temperatures of the GaN channel/buffer layers and the top  $\sim$ 6  $\mu$ m of the SiC substrate. The temperature of the AlN transition layer could not be probed due to the low intensity and signal-to-noise ratio resulting from the small layer thickness. For the AlGaN HEMTs, it was possible to probe the average temperatures of the Al<sub>0.30</sub>Ga<sub>0.70</sub>N channel/ buffer layers, the AlN transition layer, and the top  $\sim$ 5  $\mu$ m of the sapphire substrate. To determine the temperature of the GaN layer, a multispectral analysis method<sup>30</sup> was used. For the remaining layers, Raman temperature calibrations were performed to determine the temperature dependence of the peak positions and linewidths of several phonon modes; the temperature calibrations consisted of measuring the peak position and linewidth at zero power dissipation through the stage temperature range of 25 °C to 175 °C in 10 °C intervals. The following Raman phonon modes and their respective spectral features were monitored: the Al<sub>0.30</sub>Ga<sub>0.70</sub>N A<sub>1</sub> (LO) peak position,<sup>31</sup> the AlN  $A_1$  (LO) peak position,<sup>31</sup> the sapphire  $A_{1g}$  peak position, and the SiC E<sub>2</sub> (TO) peak position. To minimize stress effects on the peak position shift<sup>32</sup> for Al<sub>0.30</sub>Ga<sub>0.70</sub>N and AlN, the A<sub>1</sub> (LO) peak position was monitored because it has been shown to be less sensitive to thermoelastic stress effects as compared to the E2 (high) peak position. 31,33 Due to larger probing volumes and smaller temperature gradients in the sapphire and SiC substrates, stress effects were assumed not to significantly impact the measured temperature results.

The dependence of bias conditions (for fixed power dissipation) on the heat generation profile and the resulting channel temperature distribution was also investigated since the channel peak temperature rise was shown to directly impact the device lifetime. The gate bias conditions were determined from the transfer characteristics of the  $Al_{0.30}Ga_{0.70}N$  HEMT [Fig. 2(a)]. The pinched-off channel condition was defined as the gate voltage which resulted in  $\sim$ 15% of the saturation drain current ( $V_{GS}=1$  V); the open channel condition was defined as the gate voltage which resulted in  $\sim$ 90% of the saturation drain current ( $V_{GS}=4$  V). For the GaN HEMTs, the open channel condition utilized the same requirement which resulted in  $V_{GS}=2$  V. The measured output characteristics of the  $Al_{0.30}Ga_{0.70}N$  channel HEMT show good agreement with the simulation results, establishing confidence in the model [Fig. 2(b)].

Comparison of the vertical temperature distributions of the  $Al_{0.30}Ga_{0.70}N$  and GaN channel HEMTs shown in Fig. 3 highlights the magnification of self-heating in the  $Al_{0.30}Ga_{0.70}N$  device due to the

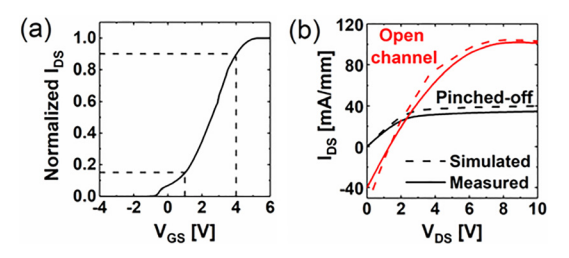


**FIG. 2.** (a) Measured transfer characteristics of the Al $_{0.30}$ Ga $_{0.70}$ N channel HEMT. The dashed lines indicate gate bias conditions for "open channel" (normalized l $_{\rm DS}\sim 0.15$ ) and "pinched-off" (normalized l $_{\rm DS}\sim 0.9$ ) conditions. (b) Measured and simulated output characteristics of the Al $_{0.30}$ Ga $_{0.70}$ N channel HEMT under open channel (V $_{\rm GS}=4$  V) and pinched-off (V $_{\rm GS}=1$  V) conditions.

increased thermal resistance resulting from the lower thermal conductivity of the  $Al_{0.30}Ga_{0.70}N$  system. Under open channel conditions, the  $Al_{0.30}Ga_{0.70}N$  HEMT ( $V_{\rm DS}=9$  V,  $P_{\rm density}=0.76$  W/mm) has a peak temperature approximately three times greater than that for the GaN HEMT ( $V_{\rm DS}=20$  V,  $P_{\rm density}=1.61$  W/mm) while operating at less than half the power density. However, this is expected due to the high thermal resistance of the  $Al_xGa_{1-x}N$ -on-sapphire system  $[k_{Al0.3Ga0.7N}\sim8.5$  W/(m\*K)] $^{34}$  as compared to GaN-on-SiC  $[k_{\rm GaN}\sim130$  W/ (m\*K)] $^{.35,36}$  Additionally, the temperature gradient in the  $Al_{0.30}Ga_{0.70}N$  channel/buffer is greater than that in the GaN channel/buffer suggesting larger thermal stress gradients in the former.

Under pinched-off conditions ( $V_{DS}=31\,V$ ,  $P_{density}=0.76\,W/mm$ ), heat generation in the  $Al_{0.30}Ga_{0.70}N$  HEMT becomes localized under the drain-side corner of the gate, whereas for open channel conditions, the heat generation is more evenly distributed across the channel length <sup>22,37</sup> [Fig. 4(a)]. The peak heat generation of the  $Al_{0.30}Ga_{0.70}N$  HEMT under open channel conditions only reaches  $\sim\!60\%$  of that under pinched-off conditions. By extending the dimensionality of the thermal analysis to probe both lateral and vertical temperature distributions, the normalized magnitude and distribution of the heat generation profile of the  $Al_{0.30}Ga_{0.70}N$  HEMT under these different bias conditions is reflected in the measured and simulated temperature profiles [Figs. 4(b) and 4(c)]. The magnitude of the vertical temperature gradient in the  $Al_{0.30}Ga_{0.70}N$  at the drain-side of the gate increases substantially as the device channel becomes pinched-off [Fig. 4(c)]. This can be understood as a marked

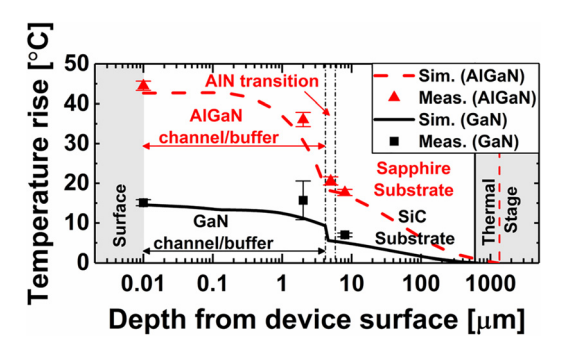


**FIG. 3.** Depth temperature distributions of the  $Al_{0.30}Ga_{0.70}N$  and GaN channel HEMTs under open channel conditions with power densities of  $0.76\,W/mm$  and  $1.61\,W/mm$ , respectively. The depth temperature distributions were measured (meas.) and simulated (sim.) at the drain-side edge of the gate.

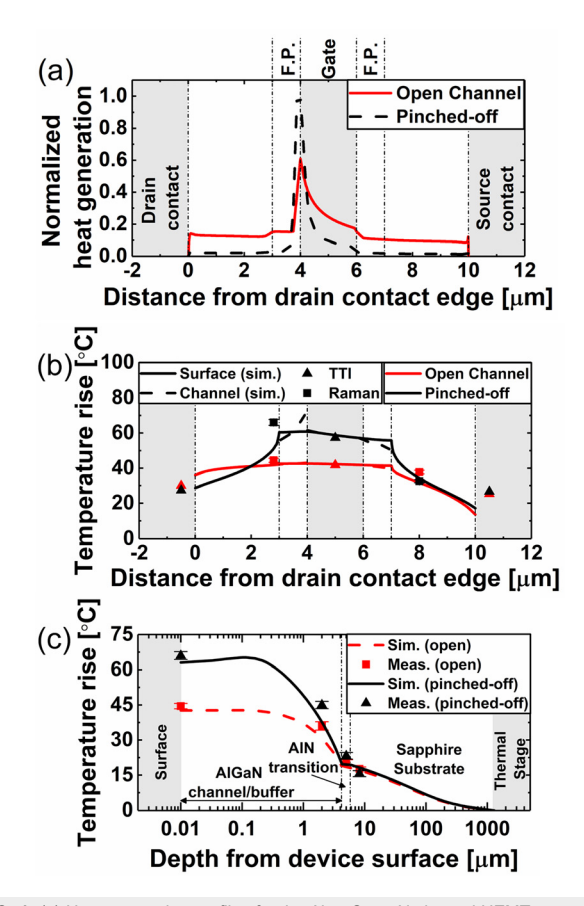


**FIG. 4.** (a) Heat generation profiles for the Al $_{0.30}$ Ga $_{0.70}$ N channel HEMT normalized with respect to the pinched-off condition for identical power densities (0.76 W/mm). (b) Lateral and (c) depth temperature distributions of the Al $_{0.30}$ Ga $_{0.70}$ N channel HEMT under open channel and pinched-off conditions for identical power densities. The depth temperature distributions were measured and simulated at the drain-side edge of the gate.

increase in the local heat flux in the active region of the device because the heat generation becomes more localized in accordance with the electric field concentration at the drain-side edge of the gate.

The electrothermal model was applied to evaluate the effectiveness of thermal management solutions developed for III-V device technologies, including both bottom-side (high thermal conductivity substrate integration<sup>38</sup>) and top-side (flip-chip integration<sup>39</sup>) approaches. As shown in Fig. 5(a), bottom-side approaches (case 2) such as selecting a high thermal conductivity substrate like diamond<sup>3</sup> and thinning the buffer layer reduce the device thermal resistance by 67%. Top-side thermal management realized through flip-chip integration to a carrier substrate<sup>39</sup> using gold bumps (cases 3 and 4) showed more promising results as reductions in thermal resistance up to 78% were achieved. This is because flip-chip integration enables heat sinking closer to the heat generation. While thermal management of the Al<sub>0.30</sub>Ga<sub>0.70</sub>N channel HEMT was very effective at reducing thermal resistance, the thermal performance was not comparable to the reference GaN HEMT (case 5) at room temperature base conditions. However, the model may not be optimized for the final

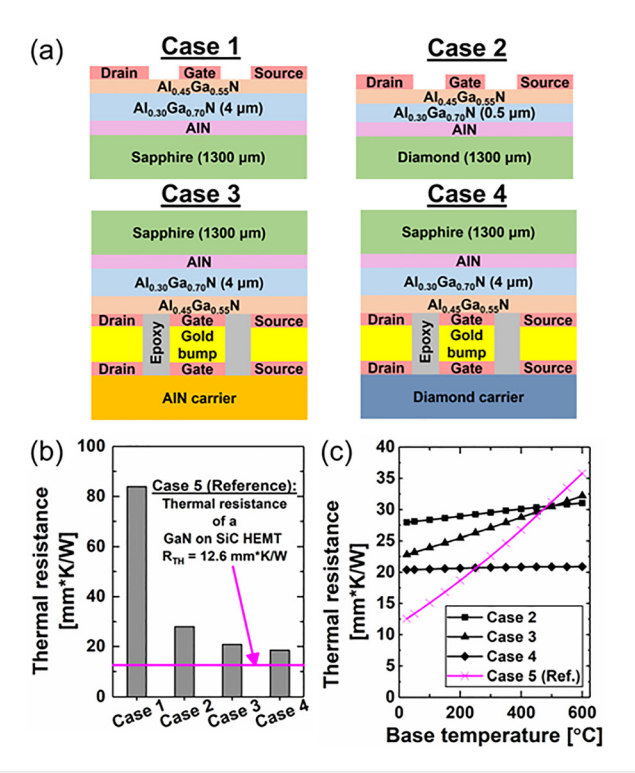


**FIG. 5.** (a) Thermal management solutions for the Al $_{0.30}$ Ga $_{0.70}$ N channel HEMT: case 1—AlGaN (4  $\mu$ m buffer) on sapphire (1300  $\mu$ m); case 2—AlGaN (0.5  $\mu$ m buffer) on diamond (1300  $\mu$ m); case 3—AlGaN (4  $\mu$ m buffer) on sapphire (1300  $\mu$ m) flip chip integrated to an AlN carrier; and case 4—AlGaN (4  $\mu$ m buffer) on sapphire (1300  $\mu$ m) flip chip integrated to a diamond carrier. A baseline case (case 5, not shown) for reference is GaN (4  $\mu$ m) on SiC (650  $\mu$ m). (b) Comparison of the thermal resistance for the various thermal management solutions at room temperature (25 °C) base conditions. The HEMT operating power density was 6 W/mm for all cases. (c) The effect of base temperature on the thermal resistance.

packaging or application. For example, the model imposes an isothermal bottom-side boundary condition of 25 °C which can be unrealistic. Because the AlGaN thermal conductivity is a much weaker function of temperature, the choice of 25 °C was very conservative since the thermal benefits of GaN over AlGaN observed here will diminish at higher temperature boundary conditions more relevant to many applications especially high temperature and extreme environment electronics.<sup>40</sup>

Accordingly, the effect of base temperature on thermal resistance in the  ${\rm Al_{0.30}Ga_{0.70}N}$  and GaN channel HEMTs was investigated and compared [Fig. 5(b)]. For all thermal management schemes, the  ${\rm Al_{0.30}Ga_{0.70}N}$  HEMT showed potential for better thermal performance than the GaN HEMT at high temperatures due to significant increases in the thermal resistance of the GaN system. To the  ${\rm Al_{0.30}Ga_{0.70}N}$  HEMT on a sapphire substrate flip chip integrated to a diamond carrier (case 4), the thermal resistance becomes less than that for the reference GaN HEMT (case 5) for base temperatures beyond 250 °C. In contrast to GaN, the combination of the ultrawide bandgap, thermal conductivity with a negligible temperature dependence, and relatively temperature insensitive electrical output characteristics  $^{2.8,42}$  make AlGaN suitable for high temperature electronics.

highlight the significant advantages that thermally optimized Al<sub>x</sub>Ga<sub>1-x</sub>N devices can have over GaN in extreme temperature environments.4

However, thermal management can negatively affect electrical performance, and electrothermal codesign is required. While diamond is the most effective substrate/carrier for thermal management [Fig. 5(a)] due to its high thermal conductivity, AlN could be more promising from economical and electrical standpoints due to lower cost and increased mobility resulting from reduced threading dislocation densities and higher crystalline quality of the Al<sub>x</sub>Ga<sub>1-x</sub>N buffer. Top-side thermal management such as flip chip integration increases parasitic capacitances, 46 lowering cutoff and maximum operational frequencies for RF applications.<sup>47</sup> Efforts to minimize these parasitic capacitances by increasing the stand-off distance between the RF chip and submount through the use of thicker bonding pads would increase the thermal resistance between the transistor channel and thermal ground, negating the benefits of flip-chip integration. This example highlights the interdependent nature of the problem and the need to consider electrical and thermal performance simultaneously. Additionally, more realistic device designs such as multifinger devices need to be considered as the benefits of the flip-chip integration used here diminishes for these devices since the contact pads are much farther from the active area of the device. However, previous studies<sup>48,49</sup> demonstrated successful electrothermal codesign of power devices which enabled multifinger AlGaN/GaN HEMTs with reduced areal footprints while improving both the electrical and thermal device performance.

In conclusion, thermal analysis of an Al<sub>0.30</sub>Ga<sub>0.70</sub>N channel HEMT was undertaken through multidimensional thermal characterization and electrothermal simulation. An increased room temperature thermal resistance due to the lower thermal conductivity of the Al<sub>x</sub>Ga<sub>1-x</sub>N system results in aggravated device self-heating and large temperature gradients through the thickness of the Al<sub>0.30</sub>Ga<sub>0.70</sub>N layer. Applying thermal management solutions established for III-V device technologies, the thermal performance of the Al<sub>0.30</sub>Ga<sub>0.70</sub>N channel HEMT can improve significantly. Although relatively inferior at room temperature, the thermal performance of thermally optimized Al<sub>0.30</sub>Ga<sub>0.70</sub>N channel HEMTs can become comparable or superior to standard GaN channel HEMTs at high ambient temperature conditions. Combined with benefits from the ultrawide bandgap and temperature insensitive electrical output characteristics, the Al<sub>x</sub>Ga<sub>1-x</sub>N device technology has potential to enable applications that require extended operation at high temperatures (350 °C-1000 °C) where active cooling is not feasible, including combustion chambers, exhaust systems of automotive/aviation engines, down-hole environments in deep-well drilling, industrial processing plants, re-entry vehicles, and satellites.

Funding for efforts by the Pennsylvania State University was provided by the AFOSR Young Investigator Program (Grant No. FA9550-17-1-0141, Program Officers: Dr. Brett Pokines and Dr. Michael Kendra, also monitored by Dr. Kenneth Goretta). Additional funding (Anushka Bansal and Joan M. Redwing) was provided by the NSF (No. DMR-1808900). Disha Talreja, Alexej Pogrebnyakov, and Venkatraman Gopalan acknowledge support from the Penn State NSF-MRSEC Center for the Nanoscale Science Grant No. DMR 1420620. Sandia National Laboratories is a multi-mission laboratory

managed and operated by the National Technology & Engineering Solutions of Sandia, LLC, a wholly owned subsidiary of Honeywell International Inc., for the U.S. Department of Energy's National Nuclear Security Administration under contract No. DE-NA0003525.

```
REFERENCES
 <sup>1</sup>T. Nanjo et al., IEEE Trans. Electron Devices 60, 1046 (2013).
 <sup>2</sup>P. H. Carey IV et al., IEEE J. Electron Devices Soc. 7, 444 (2019).
 <sup>3</sup>M. E. Coltrin et al., ECS J. Solid State Sci. Technol. 6, S3114 (2017).
 <sup>4</sup>A. Raman et al., Jpn. J. Appl. Phys., Part 1 47, 3359 (2008).
 <sup>5</sup>R. J. Kaplar et al., IEEE Power Electron. Mag. 4, 36 (2017).
 <sup>6</sup>R. J. Kaplar et al., ECS J. Solid State Sci. Technol. 6, Q3061 (2017).
 <sup>7</sup>S. Hashimoto et al., Phys. Status Solidi C 7, 1938 (2010).
 <sup>8</sup>B. A. Klein et al., ECS J. Solid State Sci. Technol. 6, S3067 (2017).
 <sup>9</sup>S. Bajaj et al., Appl. Phys. Lett. 109, 133508 (2016).
<sup>10</sup>E. A. Douglas et al., Phys. Status Solidi A 214, 1600842 (2017).
<sup>11</sup>T. Razzak, H. Xue, Z. Xia, S. Hwang, A. Khan, W. Lu, and S. Rajan, in IMWS-
AMP (IEEE, 2018). 122A. G. Baca et al., ECS J. Solid State Sci. Technol. 6, S3010 (2017).
<sup>13</sup>X. D. Wang et al., IEEE Trans. Electron Devices 59, 1393 (2012).
<sup>14</sup>A. Venkatachalam et al., Semicond. Sci. Technol. 26, 085027 (2011).
<sup>15</sup>A. Sarua et al., IEEE Trans. Electron Devices 53, 2438 (2006).
<sup>16</sup>A. Christensen et al., IEEE Trans. Electron Devices 52, 1683 (2005).
<sup>17</sup>G. J. Riedel et al., IEEE Electron Device Lett. 30, 103 (2009).
<sup>18</sup>T. J. Anderson et al., ECS J. Solid State Sci. Technol. 6, Q3036 (2017).
<sup>19</sup>X. Chen et al., IEEE Trans. Electron Devices 61, 4056 (2014).
<sup>20</sup>Y. Won et al., IEEE Trans. Compon., Packag., Manuf. Technol. 5, 737 (2015).
<sup>21</sup>S. Karmalkar and U. K. Mishra, IEEE Trans. Electron Devices 48, 1515 (2001).
<sup>22</sup>S. Choi et al., IEEE Trans. Electron Devices 60, 159 (2013).
23B. Chatterjee, J. S. Lundh, J. Dallas, H. Kim, and S. Choi, in ITherm (IEEE,
  2017), pp. 1247-1252.
<sup>24</sup>D. K. Schroder, Semiconductor Material and Device Characterization (John
  Wiley & Sons, 2006).
<sup>25</sup>A. J. Schmidt et al., Rev. Sci. Instrum. 80, 094901 (2009).
<sup>26</sup>D. Kendig, A. Tay, and A. Shakouri, in THERMINIC (IEEE, 2016), pp. 115–120.
<sup>27</sup>A. Shakouri, A. Ziabari, D. Kendig, J.-H. Bahk, Y. Xuan, D. Y. Peide, K.
  Yazawa, and A. Shakouri, in SEMI-THERM (IEEE, 2016), pp. 128-132.
<sup>28</sup>J. Dallas et al., Appl. Phys. Lett. 112, 073503 (2018).
<sup>29</sup>N. J. Everall, Appl. Spectrosc. 63, 245A (2009).
30 S. Choi et al., IEEE Trans. Electron Devices 60, 1898 (2013).
<sup>31</sup>M. Kuball, Surf. Interface Anal. 31, 987 (2001).
32T. Beechem et al., J. Appl. Phys. 103, 124501 (2008).
33 T. Batten et al., J. Appl. Phys. 106, 094509 (2009).
34B. C. Daly et al., J. Appl. Phys. 92, 3820 (2002).
35 T. E. Beechem et al., J. Appl. Phys. 120, 095104 (2016).
36 E. Ziade et al., Appl. Phys. Lett. 110, 031903 (2017).
<sup>37</sup>E. Heller et al., Microelectron. Reliab. 53, 872 (2013).
38H. C. Nochetto, N. R. Jankowski, and A. Bar-Cohen, in CSICS (IEEE, 2012),
pp. 1-4.
<sup>39</sup>S. Choi et al., IEEE Trans. Compon., Packag., Manuf. Technol. 6, 740
  (2016).
<sup>40</sup>M. A. Huque et al., Solid. State. Electron. 53, 341 (2009).
<sup>41</sup>W. Liu and A. A. Balandin, J. Appl. Phys. 97, 073710 (2005).
<sup>42</sup>H. Tokuda et al., Appl. Phys. Express 3, 121003 (2010).
<sup>43</sup>E. R. Heller, IEEE Trans. Electron Devices 55, 2554 (2008).
44 J. D. Cressler and H. A. Mantooth, Extreme Environment Electronics (CRC
  Press, 2017).
45K. Son et al., Nanosci. Nanotechnol. Lett. 2, 89 (2010).
<sup>46</sup>D. M. Pozar, Microwave Engineering (John Wiley & Sons, 2009).
```

47W. Lu et al., Solid. State. Electron. 46, 1441 (2002).

<sup>49</sup>S. K. Oh *et al.*, Appl. Phys. Express **10**, 016502 (2017).

<sup>48</sup>S. K. Oh et al., IEEE Trans. Electron Devices **63**, 620 (2016).